Enhanced LR-FHSS receiver for headerless frame recovery in space–terrestrial integrated IoT networks

Diego Maldonado, Leonardo S Cardoso, Juan Andrés A Fraire, Alexandre Guitton, Oana Iova, Megumi Kaneko, Hervé Rivano

Computer Networks 257 (2025) 111018

Contents lists available at ScienceDirect

Computer Networks

journal homepage: www.elsevier.com/locate/comnet

Enhanced LR-FHSS receiver for headerless frame recovery in space–terrestrial integrated IoT networks

Diego Maldonado [a], Leonardo S. Cardoso [a], Juan A. Fraire [a,b,*], Alexandre Guitton [c], Oana Iova [a], Megumi Kaneko [d], Hervé Rivano [a]

[a] Inria, INSA Lyon, CITI, UR3720, 69621 Villeurbanne, France
[b] CONICET - Universidad Nacional de Córdoba, Córdoba, Argentina
[c] Université Clermont-Auvergne, CNRS, Clermont-Auvergne-INP, LIMOS, 63000, Clermont-Ferrand, France
[d] National Institute of Informatics (NII), Tokyo 101-8430, Japan

ARTICLE INFO

Keywords:
Low power wide area networks
Long-range frequency hopping spread spectrum
LoRa/loRaWAN

ABSTRACT

Long-Range Frequency Hopping Spread Spectrum (LR-FHSS) is a recent IoT modulation technique designed for communication between low-power ground end-devices and Low-Earth Orbit (LEO) satellites. To successfully decode a frame, an LR-FHSS gateway must receive at least one header replica and a substantial portion of the payload fragments. However, the likelihood of LR-FHSS header loss increases with the number of concurrent transmissions. Moreover, Doppler effects (such as the Doppler shift and the Doppler rate) distort the signals the satellites receive. This paper investigates advanced receiver techniques for recovering LR-FHSS frames with lost headers characterized by significant Doppler effects. This paper's main contribution is specifying and validating a novel LR-FHSS receiver model for space–terrestrial integrated IoT environments. Obtained simulation results prove that our enhanced LR-FHSS receiver can decode a significant portion of the missing frames, improving the overall throughput achievable by using the legacy LR-FHSS receiver.

1. Introduction

Direct-to-Satellite Internet of Things (DtS-IoT) is a novel approach to integrated terrestrial and spatial wireless communications where small low-energy devices on Earth directly communicate with a Low Earth Orbit (LEO) satellite [1]. Small satellites, including affordable CubeSats, enable the establishment of dependable and cost-effective networks by relaying packets to ground stations, possibly through other satellites forming a constellation [2]. DtS-IoT is inherently more sustainable, relying on a small number of nano-satellites and low-power, battery-operated ground terminals, typically consuming power in the milliwatt range. This contrasts broadband mega-constellations such as Starlink, which require thousands of large spacecraft and power-hungry end-user terminals that are significantly more power-hungry, consuming tens of watts [3]. However, this sustainability comes with trade-offs, including lower data rates, higher latencies, and reduced data volumes, characteristic of IoT applications.

Conventional Low-Power Wide Area Network (LPWAN) technologies [4], such as LoRa and LoRaWAN, typically employed in urban and rural applications, have been recently updated to support DtS-IoT networks [5]. Furthermore, adopting open standards like LoRaWAN facilitates the unrestricted deployment of LoRa networks, as they comply with regional regulations. When coupled with CubeSats, this approach offers an economical alternative for building satellite networks that is competitive with available low-power, low-data rate satellite solutions (e.g., Argos [6], APRS [7], S-AIS [8], and ADS-B [9]). Moreover, since it is inherently integrated with terrestrial networks, it offers a seamless transition for mobile low-energy devices in applications such as asset tracking. The primary challenge in extending LPWANs to the DtS-IoT domain lies in effectively scaling the medium access schemes to manage the expansive coverage footprint of LEO satellites.

The Long-Range Frequency Hopping Spread Spectrum (LR-FHSS) modulation is the newest addition to the LPWAN technologies, designed explicitly by Semtech for low-power devices communicating with LEO satellites [10]. This modulation has the advantage of being compatible with existing terrestrial LoRaWAN networks. Through a simple firmware update of LoRaWAN 2nd generation or version 2 gateways, end devices using the new LR-FHSS modulation can operate alongside legacy LoRa modulation, facilitating the adoption of LR-FHSS. To increase robustness against interference, LR-FHSS combines several techniques: (1) *packet fragmentation*: the payload is split into several smaller fragments, each one lasting 102.4 ms; (2) *error correction*: the payload is encoded such that it can still be recovered even if a large

* Corresponding author at: Inria, INSA Lyon, CITI, UR3720, 69621 Villeurbanne, France.
E-mail address: juan.fraire@inria.fr (J.A. Fraire).

https://doi.org/10.1016/j.comnet.2024.111018
Received 5 July 2024; Received in revised form 2 October 2024; Accepted 23 December 2024
Available online 31 December 2024

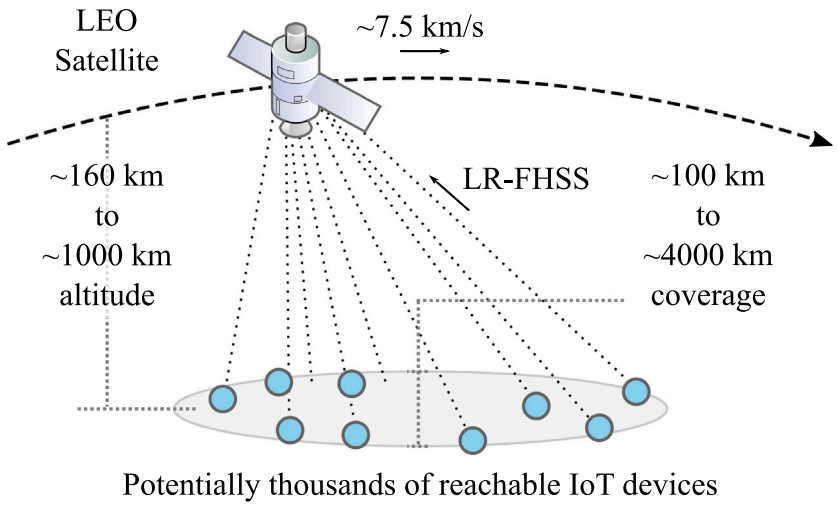

Fig. 1. Direct-to-Satellite IoT scenario.

proportion of the fragments are lost, and (3) *frequency hopping*: payload fragments are sent on random narrow-band sub-channels (488 Hz bandwidth); the hopping sequence index is encoded in the frame header, and this header is sent as multiple replicas on random sub-channels. Successful decoding of an LR-FHSS packet requires the reception of at least one header replica and a significant portion of the fragments. This approach allows a LoRaWAN gateway on a LEO satellite to decode hundreds of simultaneous LR-FHSS transmissions [11,12], meeting DtS-IoT communication scalability requirements (see Fig. 1).

Even with the enhanced features of LR-FHSS, one of the primary obstacles encountered in DtS-IoT networks remains the network's scalability, particularly in situations where thousands of end devices must be served by a single satellite (e.g., in asset tracking, environmental monitoring, smart metering, agriculture, utilities). It has been shown that one of the leading causes for LR-FHSS frame loss is due to header loss, especially when the Coding Rate (CR) imposes fewer header repetitions [12–14]. Fraire et al. proposed a mechanism enabling the decoding of headerless frames, based on a greedy approach [14]. However, the authors did not account for the specific characteristics of satellite communications, such as Doppler effects. They based their model on strict assumptions, such as an identical size for all frames, the loss of all headers, and a coarse time model that hinders the approach's practical applicability.

We address critical Doppler limitations in existing methods and define an enhanced LR-FHSS receiver architecture capable of extending LR-FHSS scalability by decoding headerless frames in space and terrestrial LoRaWAN networks. Specifically, our main contributions are as follows:

1. We define realistic modeling of the physical channel by considering the specific characteristics of the space–terrestrial communications environment, such as Doppler effects.
2. We propose a new algorithm for headerless frame recovery in LR-FHSS by considering Doppler effects and relaxing some of the strict assumptions previously made in previous works. We account for mixed payload sizes and do not assume all headers are lost.
3. We propose a novel Enhanced Decoder architecture for space–terrestrial LR-FHSS gateways to enhance the decoding rate of a traditional LR-FHSS gateway by including the headerless frame recovery algorithm in the decision process and by proposing a decoder design that accounts for both coding rates.

The paper is structured as follows. Section 2 provides background information on related works in scaling LR-FHSS. Section 3 details the system model considering the space–terrestrial channel. The enhanced LR-FHSS receiver architecture is presented in Section 4. Section 5 presents the simulation scenario and results. Section 6 initiates a discussion on our proposal and sets the direction for future efforts in scaling LR-FHSS. Finally, Section 7 summarizes the conclusions of this paper.

2. Related work

2.1. Background on DtS-IoT and LR-FHSS

LEO satellites are crucial in extending IoT coverage to remote and geographically challenging areas where terrestrial infrastructure is insufficient [5]. Due to their proximity to Earth, LEO satellites offer lower transmission delays and power requirements compared to geostationary satellites. As IoT device numbers increase, scalable and reliable communication protocols, such as DtS-IoT [1], are needed to meet global connectivity demands. DtS-IoT is a more sustainable solution, relying on low-power, low-data-rate devices [15]. LR-FHSS [10] has emerged as a promising technique to enhance scalability by minimizing self-interference while maintaining a robust link budget. Recent research on LR-FHSS focuses on performance analysis [11,16], outage probabilities [13,17], energy efficient [18], recovery methods [14], transceiver design [19], simulators [20], network coding [21], content resolution [22], and experimental data collection from ground test beds [23].

2.2. Background on LR-FHSS scalability

Considering the large fields of view of LEO satellites, packet collision is a much more challenging issue in space DtS-IoT than in terrestrial networks. Even though LR-FHSS enhanced the scalability of legacy LoRaWAN concerning terrestrial networks, pushing scalability limits further as needed in DtS-IoT remains an open challenge not addressed by the recent publications listed in the section above. Indeed, the state-of-the-art specifically focused on LR-FHSS scalability is limited. As discussed below, researchers focused mainly on reducing collisions by optimizing the frequency hopping sequence (FHS) and recovering LR-FHSS frames despite losing all header replicas.

Optimizing the FHS. The FHS is a crucial element that impacts the scalability of LR-FHSS, as it fundamentally determines how many fragments from different LR-FHSS frames overlap. The relationship between the possible FHSs and the extraction rate of colliding frames encompasses the intricate interplay between LR-FHSS's error correction mechanisms and the mandatory frequency shifts dictated by grid definitions. However, to our knowledge, limited research exists on the design of appropriate FHS techniques for LR-FHSS. One example is

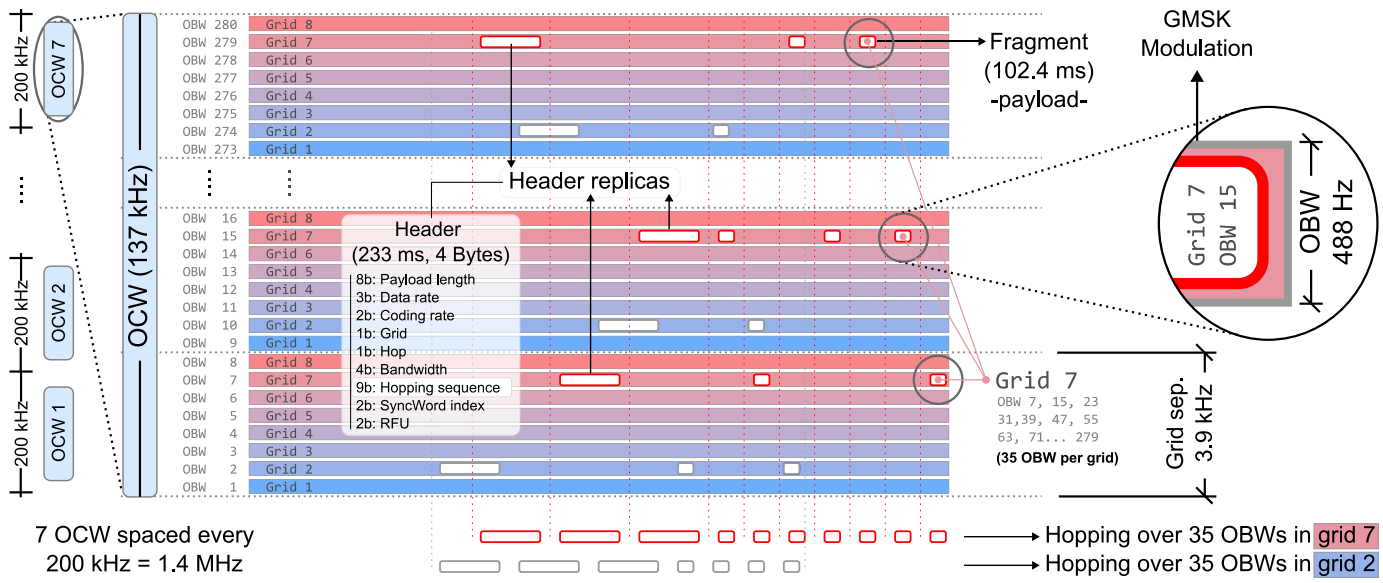

Fig. 2. LR-FHSS time–frequency depiction (adapted from [14]). All the header replicas and fragments of an LR-FHSS frame need to do frequency hopping over OBWs belonging to the same grid. Header replicas maximize the header decoding rate but generate more congestion and become the main reason for frame loss, as shown in [14].

the research on the Wide-Gap FHS (WGFHS) family addressed in [24]. Also, Zhang et al. proposed a dynamic frequency hopping method that accounts for the changing SNR values of the sub-channels [25]. Wang et al. on the other hand, proposed a frequency hopping design that incorporates segment-level coding in a high-order Galois field with erasure detection to enhance immunity against clustered errors [26].

Recovering headerless frames. Recent research has demonstrated that header collision is the primary cause of frame loss in congested LR-FHSS channels. This collision results in the loss of header replicas, rendering it impossible to successfully decode the subsequent payload fragments. The header fragility problem has been highlighted as the primary limitation in LR-FHSS scalability in several works [12–14]. One identified reason is the inefficiency of repetition codes, prompting Knop et al. to propose combining header replicas from multiple packets sent by the same user [27]. Still, when all header replicas are lost, none of these approaches tries to recover the frames. Recent work in [14] proposed a Mixed Integer Linear Programming (MILP) formulation and a heuristic approach to optimize the allocation of FHS in the dictionary to a series of payload fragments lacking an associated LR-FHSS header. However, this approach has several limitations, including the omission of Doppler effects — a significant issue in space and satellite communications — and the assumption that all headers are absent in the receiver decoding matrix, whereas, in practice, a combination of successful and lost headers is present.

This paper proposes a definitive approach to headerless LR-FHSS decoding that addresses the limitations above. To demonstrate the practical applicability of our proposal, we present an architecture for a headerless-capable LR-FHSS receiver, building on the existing transceiver designs proposed by the community [28,29]. To properly frame our contribution, the following subsections describe the details of LR-FHSS modulation, the challenges imposed by the highly dynamic space–terrestrial channel, and the associated headerless LR-FHSS decoding techniques.

3. System model

In this section, we present the model of LR-FHSS transmissions at the physical layer in a Direct-to-Satellite scenario with the Doppler Effect affecting transmissions.

3.1. LR-FHSS modulation model

LR-FHSS is a new modulation technique that rapidly uses several narrow-band channels to hop frequencies within a single frame. Primarily tailored for uplink communications, LR-FHSS proves particularly efficient when many energy-limited devices transmit simultaneously to LEO satellites, thanks to the large number of narrow-band channels LR-FHSS uses.

LR-FHSS segments the frequency band into a few channels called Occupied Channel Widths (OCWs). Each OCW is further partitioned into multiple narrow-band channels called Occupied Bandwidths (OBWs) [11]. OBWs are further regrouped into grids, sets of non-consecutive OBWs separated by a minimum distance. Details on the OCW channel bandwidth, OBW channel count, and the number of grids specified for LR-FHSS are provided in [10]. Note that the large number of OBW channels (between 280 and 3120) is the core enabler of LR-FHSS's scalability. Fig. 2 illustrates the structure and critical information of the LR-FHSS framing. Frame transmission initiates with multiple header copies, called replicas, each lasting 233 ms in airtime. Depending on the chosen data rate scheme, the header is replicated two or three times to ensure reliable reception. Note that a single replica needs to be received to decode the header. Replicas are followed by the segmented payload, where each segment, called a fragment, lasts 102.4 ms in airtime. These replicas and fragments are relayed over varying OBWs within a single grid, according to the Frequency Hopping Sequence (FHS). Each header replica conveys the index of the chosen FHS. The diversity of possible sequences (either 384 for the US1523 or EU137 regions or 512 for the EU336 region, more details in [10]), combined with the large number of OBWs, significantly reduces the likelihood of multiple frames adopting the same hopping sequence and thus wholly overlapping. Moreover, payload encoding is designed to keep data integrity intact even with substantial fragment loss [11]. The LoRaWAN standard prescribes two LR-FHSS configurations:

- *Robust Configuration*: Headers are transmitted three times, and the payload is encoded at CR = 1/3 (denoted as CR1 in this work), meaning that successful frame recovery demands a minimum of 33% fragment decoding.
- *Fast Configuration*: Headers are transmitted twice, and the payload is encoded at CR = 2/3 (denoted as CR2 in this work), meaning that successful frame recovery demands a minimum of 67% fragment decoding.

3.2. Signal and channel model for LEO orbits

In this work, two related propagation models are used: (i) a *power-centric* model, used to understand the behavior of the collision from an interference perspective, and (ii) a *collision-centric* model, which is a simplification of the power-centric model and is mainly used to offload more complex analysis when deemed unnecessary. We focus on a single OCW for both models to simplify the approach without losing generality. Since OCWs do not overlap, extending this model to multiple OCWs is straightforward, as it involves instantiating separate models for every OCW channel.

3.2.1. Power-centric model

The Gaussian Minimum Shift Keying (GMSK) modulation transmits LR-FHSS packets. Since decoding is not the focus of this work, we can simplify our physical layer model by abstaining from the actual transmission of information and focusing on the power of the transmitted signals. GMSK is a constant-amplitude modulation so that we can estimate the signal power per symbol as the square of the modulus of the complex-valued symbol. This power estimation is done for both headers and fragments in their time–frequency representation, with the power equally distributed over the OBW sub-channel. We assume no shadowing or small-scale fading in the channel model, as in [14]. Therefore, the power received by the LEO satellite from the ith end-device P_i is computed as

$$P_i = P_{\mathrm{t}} \cdot G_{\mathrm{r}} \cdot G_{\mathrm{t}} \cdot \mathrm{Pl}(d_i, f_{\mathrm{c}}), \tag{1}$$

where P_{t}, G_{r} and G_{t} are the transmission power, the receiver antenna gain, and the transmitter antenna gain for the ith device, respectively. $\mathrm{Pl}(d_i, f_{\mathrm{c}})$ is the free space path loss computed from the Friis formula, which depends on d_i the distance from the ith end-device to the satellite and f_{c} the carrier frequency. Since all end-devices are considered the same P_{t}, G_{r} and G_{t} are the same for all devices, hence the lack of the i index. For simplicity, we do not consider propagation losses in the atmosphere due to absorption. Finally, at the satellite receiver, we consider noise equal to the noise floor per specifications available in the Application Note documentation from Semtech [30].

3.2.2. Collision-centric model

In this simplified model, we consider three possible outcomes: (i) no signal, (ii) a single signal, and (iii) collided signals. While simulations always know incoming signals, real-world scenarios are more complex and require robust collision detection mechanisms to differentiate between single and collided signals. In [29], the authors propose several interference management techniques, proving their effectiveness in determining whether each symbol from a fragment is either collided or successfully received without interference. Our collision-centric model assumes these techniques are valid and operates under the assumption that all signals are above the noise level.

3.3. Interference, collision, and capture effect

For power-centric and collision-centric models, headers and fragments interfere when they overlap in time and frequency (i.e., fall onto overlapping OBWs). Throughout this work, the term *collision* is used to designate all headers and fragments that interfere and cannot be decoded as a consequence.

In actual transmissions, interfering signals can experience the capture effect, in which headers and fragments that fully or partially overlap in time and frequency with a favorable power ratio might allow for perfect decoding of the higher-powered one. Here, we consider the worst-case scenario in which, if the overlap is present, collision ensues regardless of the overlap extent or power ratio between the interfered signals. It should be noted that while channel sensing can detect collisions, we consider that under our assumptions, the recovery of collided fragments is impossible; hence, the capture effect is not considered in this work. Considering the capture effect and advanced collision determination and avoidance techniques such as the ones presented in [29], it would be possible to decode even more fragments and thus further increase the throughput.

Based on the received power and given the constant envelope of the GMSK used for the LR-FHSS transmissions, SINR-based collision detection techniques can be used to determine if a given header or fragment is collided or not, such as the ones proposed by Temim et al. [29]. Our proposed model assumes such techniques are implemented and can be used to rule out collisions at the symbol level.

3.4. Doppler effect model

The Doppler effect significantly influences satellite communications by introducing frequency shifts as satellites move relative to ground stations and end devices. These shifts can distort signals, degrade signal-to-noise ratio, and cause synchronization errors. Doppler compensation techniques are employed to mitigate these effects, adjusting transmitted frequencies dynamically. In the context of DtS-IoT, specifically when considering satellites in the LEO orbit, Doppler shifts are considerable due to the high orbital velocities (e.g., in the order of 7 km/s in LEO) concerning the relatively static end devices on the ground.

To reason about Doppler, let H be the satellite altitude, R the radius of the earth, g the acceleration of gravity on the surface, c the speed of light in vacuum, f_c the carrier frequency, v the satellite's velocity. Let also $x = 1 + H/R$. The Doppler frequency shift f_d is given by

$$f_d = \frac{f_c}{c}\sqrt{\frac{gR}{x}} \cdot \frac{\sin(\phi)}{\sqrt{x^2 - 2 \cdot x \cdot \cos(\phi) + 1}}, \tag{2}$$

discussed in detail in [31], where

$$\phi = t\sqrt{\frac{g}{Rx^3}}. \tag{3}$$

Consider the scenario depicted in Fig. 1, with a satellite orbiting at an altitude of $H = 600$ km providing support to 100 end-devices on the ground, distributed uniformly. Assuming the carrier signal for LR-FHSS transmissions is at $f_c = 868$ MHz (European Regional configuration [32]), Fig. 3 shows the Doppler shift seen from the satellite as it passes over the considered region. The Doppler shift is −20 kHz when the satellite approaches from the horizon (at $t = -400$), reaches 0 kHz when the satellite is directly above the region (at $t = 0$), and then increases again until 20 kHz as it moves away from the devices (at $t = 400$). This behavior has been observed in several studies, including by Ali et al. [33]. The Doppler rate is defined as the variation of the Doppler shift over time and is illustrated in Fig. 3. The peak Doppler rate is when the satellite is beyond $t = 0$ (zenithal position) and when the Doppler shift is 0.

3.4.1. Doppler in LR-FHSS with LEO

According to Semtech, LR-FHSS is specifically designed to tolerate frequency offset (directly related to Doppler shift) and frequency drift (directly related to Doppler rate) to cope with the Doppler effect observed in LEO satellite communications. To assess this claim, we simulated a 200 kHz receiver bandwidth, with end-devices sending LR-FHSS frames within an OCW with a bandwidth of 137 kHz (more detail on the simulation environment is provided in Section 4) in the LEO scenario. The minimum SNR is 10 dB. The resulting time–frequency spectrogram is presented in Fig. 4. The received signal power is computed as given by Eq. (1).

Due to the Doppler shift, we can observe how some frames fall outside the originally transmitted 137 MHz band (indicated with yellow horizontal lines). Our simulation validates that a larger receiver window of 200 MHz makes LR-FHSS tolerant to the Frequency Shift in DtS IoT scenarios. The Frequency Offset tolerance in LR-FHSS is 31.65 kHz (as reported by Semtech in Table 9 from [10]). The same

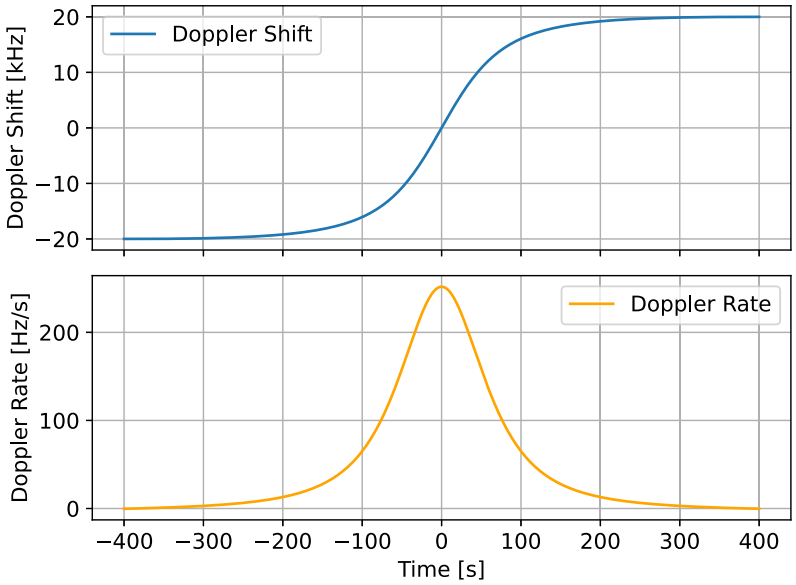

Fig. 3. Doppler shift and Doppler rate in DtS-IoT, for an altitude of 600 km and a center frequency of 868 MHz.

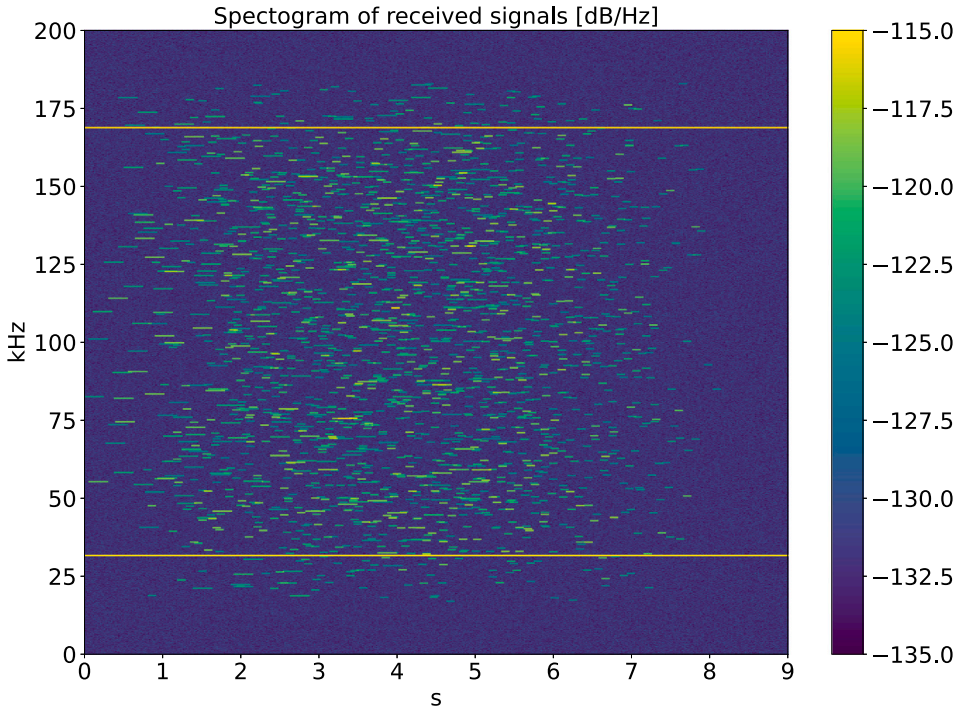

Fig. 4. Spectrogram of 100 received LR-FHSS transmissions.

work indicates that for LR-FHSS, a frequency drift of up to 100 Hz/s does not cause observable performance degradation, and a frequency drift of up to 300 Hz/s causes performance degradation of up to 1.5 dB [10]. By observing Fig. 3 and assuming that Semtech's report is accurate, the Doppler simulation results show no degradation should be observed in LR-FHSS before $t = -80$ and after $t = 80$, where the Doppler Rate is under 100 Hz/s. However, a performance degradation of up to 1.5 dB may only occur around $t = 0$ when the satellite passes just over the device on the ground.

Fig. 5 shows a closer look at the spectrogram of received frames without Doppler shift (on the left) and with Doppler shift (on the right). The spectrogram on the left could represent a typical terrestrial network with a static gateway. However, the spectrogram on the right represents what would happen in a typical DtS-IoT with a fast-moving LEO satellite when the Doppler effect is significant. Note that without the Doppler effect (on the left), the received frames are all aligned in terms of OBW (left axis), while with the Doppler effect (on the right), they are misaligned, with nonexistent OBW boundaries. It is important to note that the Power-Centric model is used to compute Figs. 4 and 5. However, the Collision-Centric model is used to introduce the LR-FHSS receiver architecture in the next section.

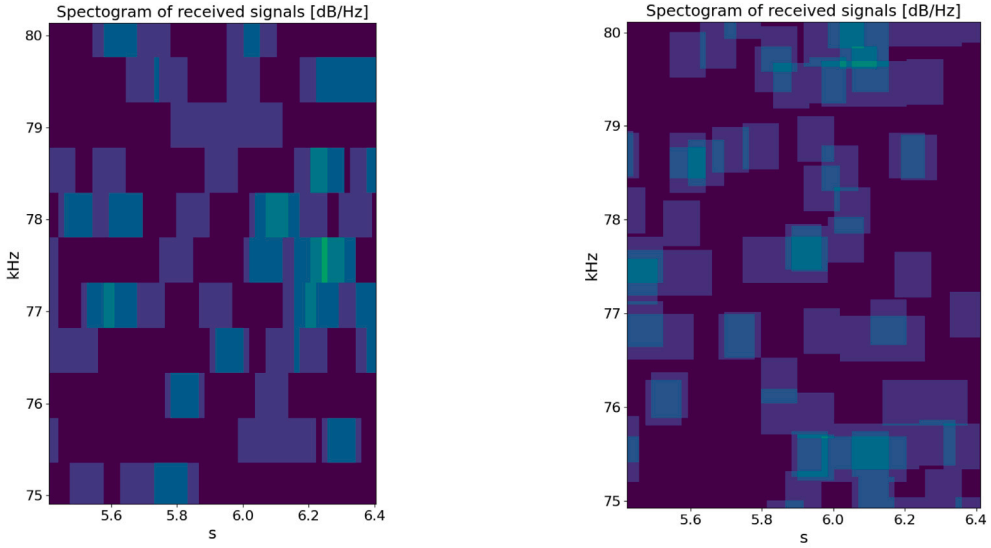

(a) Terrestrial (no Doppler shift) (b) DtS-IoT (with Doppler shift)

Fig. 5. Comparison of received LR-FHSS frames, terrestrial vs. DtS-IoT scenarios.

3.5. Practical perspective of system model assumptions

The following assumptions are incorporated into the proposed System Model to simplify the analysis and implementation in resource-constrained onboard computers while preserving the critical characteristics of LEO satellite signal propagation. These assumptions were carefully selected to ensure the model remains practical and applicable in real-world scenarios, particularly for DtS-IoT networks.

1. **No Small-Scale Fading:** In line with previous works on satellite IoT communications, the model assumes no small-scale fading or shadowing effects in the channel. While this assumption simplifies the propagation environment, it remains reasonable, as small-scale fading has a limited impact in the relatively open-space environment between ground terminals and LEO satellites.
2. **No Atmospheric Losses:** Atmospheric propagation losses due to absorption are not considered in this model. This assumption is a valid approximation for the frequencies used in LR-FHSS, as absorption is minimal at these ranges. Therefore, the focus on free-space path loss does not significantly impact the model's accuracy.
3. **Collision Handling Assumptions:** The collision-centric model assumes robust collision detection mechanisms, which are practical and feasible based on current research in interference management techniques. These methods, as proposed in [29], are grounded in real-world implementations.
4. **Doppler Effects:** Unlike previous works that overlook Doppler shift, our model explicitly accounts for Doppler effects, which are significant in LEO satellite communications due to the high orbital velocities.
5. **Simplified Fragment Collisions:** The assumption that collisions occur when fragments overlap in time and frequency is grounded in practical satellite communication conditions. Although we assume no recovery of collided fragments, this reflects the worst-case scenario.

4. Enhanced LR-FHSS receiver architecture

This section contains the details of our proposed Enhanced LR-FHSS Receiver model, describing each module in detail in the following subsections.

4.1. Headerless frame decoding

A significant cause for losing LR-FHSS frames is the collision of headers, as shown by Fraire et al. [14]. The authors proposed a mechanism enabling the decoding of headerless frames based on a greedy approach. However, the authors did not account for satellite communications' specific characteristics, such as Doppler effects, and based their model on strict assumptions. The proposed Greedy Headerless Decoding heuristic, listed in Algorithm 1, processes each time slot t sequentially. For each of the 384 known sequences, it checks if matrix M contains a transmission starting at time slot t with sequence s. If such a transmission exists, (s, t, P) is added to $\hat{T}$, where P is the length of the sequence s. This greedy heuristic has a time complexity of $\mathcal{O}(T \cdot S \cdot P)$ when the entire matrix M is known in advance, as the primary operation involves three nested loops: the first loop (line 2) runs T times, the second loop (line 3) runs S times, and the third loop (line 5) runs P times. Indeed, the principal operation of line 6 is performed within three nested `for` loops.

Algorithm 1 Greedy Headerless Decoding Heuristic (from [14]).

Require: T, S, P and M
1: $\hat{T} \leftarrow \{\}$
2: **for** $t \in [1; T]$ **do**
3: **for** $s \in S$ **do**
4: $found \leftarrow true$
5: **for** $p \in [1; P]$ **do**
6: **if** $M[t + p - 1][s[p - 1]] \neq 1$ **then**
7: $found \leftarrow false$
8: **end if**
9: **end for**
10: **if** $found = true$ **then**
11: $\hat{T} \leftarrow \hat{T} \cup \{(s, t, P)\}$
12: **end if**
13: **end for**
14: return $\hat{T}$
15: **end for**

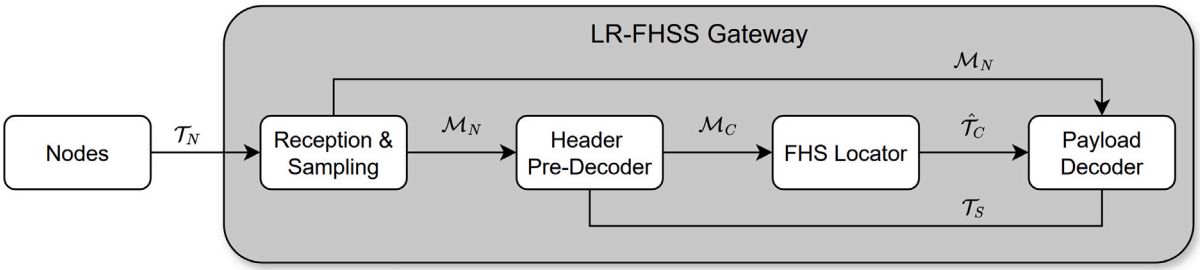

Fig. 6. LR-FHSS gateway model with Enhanced receiver.

4.2. Enhanced LR-FHSS receiver architecture

To retrieve lost payloads from LR-FHSS frames, we propose here an enhanced LR-FHSS receiver with the above-mentioned Greedy Headerless Decoding heuristic at its core. We improved this heuristic by taking into account the specific characteristics of satellite communications and relaxing several of their model assumptions, as we present next. The diagram in Fig. 6 represents a generic LR-FHSS gateway (shaded block) receiving frames from end-devices. The diagram depicts the end-to-end communication process with the following steps:

1. The end-devices transmit N LR-FHSS frames with a single Coding Rate and variable payload length (the number of payload fragments being within the range $[P_{min}, P_{max}]$) over a given time. The set of transmissions is represented by $\mathcal{T}_N$.
2. The gateway module opens a reception window of bandwidth BW during a given time window. The data is sampled in F frequency slots and T time slots, and the resulting matrix $\mathcal{M}_N$ is stored in the buffer [29]. Matrix $\mathcal{M}_N$ contains all the received LR-FHSS packets.
3. The *Header Pre-Decoder* module identifies the set of transmissions whose header is successfully received, i.e., at least one replica can be decoded, denoted as $\mathcal{T}_S$.
4. The *FHS Locator* module then infers an approximation of the set of transmissions whose header part is unsuccessfully received, *i.e.*, all headers are collided, denoted as $\hat{\mathcal{T}}_C$. Note that it is difficult to know $\mathcal{T}_C$ exactly, as the header information is missing, and thus the gateway has no information on the FHS used for the fragments.
5. Finally, the *Payload Decoder* module receives as input the original sampled matrix $\mathcal{M}_N$, the transmission set $\mathcal{T}_S$ and the uncertain collision set $\hat{\mathcal{T}}_C$, and performs the payload decoding process.

In the following subsections, we detail the proposed implementation of each enhanced LR-FHSS receiver module.

4.2.1. Reception and Sampling

The Reception and Sampling block is based on the classic LR-FHSS receiver. Jung et al. presented a detailed transceiver model for LR-FHSS-based DtS-IoT scenarios [28]. The received signals are sampled from this block in the matrix M_N.

4.2.2. Header Pre-Decoder

The Header Pre-Decoder module has two objectives. The first objective is to retrieve successfully received replicas from $\mathcal{M}_N$, similar to the traditional LR-FHSS decoder. The set of transmissions whose header was decoded, regardless of the payload status, is represented by $\mathcal{T}_S$. The second objective is to construct a secondary matrix $\mathcal{M}_S$ from $\mathcal{T}_S$, incorporating Doppler shift adjustments as in the original matrix. As the header was decoded, the FHS is known, and the frequency shift can be determined. Then, $\mathcal{M}_S$ can be subtracted from the original $\mathcal{M}_N$ following the next steps:

1. Pre-processing of $\mathcal{M}_N$: matrix $\mathcal{M}_N$ is filtered according to the status of each time slot, either idle (represented by the value 0, meaning no signal or noise), successful (represented by the value 1, meaning a single signal is present) or collided (represented by the value 2, meaning 2 or more colliding signals). This filtering process is simulated based on the number of signals per time slot. In a realistic implementation (i.e., not simulated), collision determination techniques for LR-FHSS receivers should be used for the filtering process, as the ones presented in [29].
2. Matrix $\mathcal{M}_S$ containing $\mathcal{T}_S$ is filtered following the same time slot status convention described before.
3. The difference matrix $\mathcal{M}_C = \mathcal{M}_N \ominus \mathcal{M}_S$ is computed based on the following rules: (1) $2 \ominus 0 = 2 \ominus 1 = 2 \ominus 2 = 2$, since the number of colliding signals is unknown, (2) $1 \ominus 1 = 0$, the only signal present was identified; (3) $1 \ominus 0 = 1$; and (4) $0 \ominus 0 = 0$.
4. Finally, matrix $\mathcal{M}_C$ is made binary, i.e., values equal to 2 become 1. This is done because the FHS Locator receives a binary matrix as input.

As a result of this process, the difference matrix $\mathcal{M}_C$ contains only the sequences with lost headers $\mathcal{T}_C$.

4.2.3. FHS Locator

The FHS Locator module infers the set of transmissions $\mathcal{T}_C$ whose headers failed to be recovered, aiming to locate each sequence in time and frequency. The inference technique is based on the Greedy Headerless Decoding Heuristic introduced in Section 4.1.

The Doppler effect in terrestrial scenarios with no mobility is negligible, thus, Algorithm 1 is suitable for the FHS Locator module. On the other hand, Doppler shifts need to be considered in satellite scenarios. It is known from Fig. 3 that the range in which a header or fragment will be shifted is between −20 kHz and 20 kHz. Dividing this by the size of the frequency slots allows us to determine the maximum and minimum shifts in frequency slots. Let D be the set of possible shifts in the frequency domain. Then, Algorithm 1 is updated to search also in frequency.

The modified version for satellite scenarios is presented in Algorithm 2. The main differences with the heuristic presented in Algorithm 1 are underlined (lines 4 and 7). Algorithm 2 has a time complexity of $\mathcal{O}(T \cdot S \cdot P \cdot |D|)$, a major modification being the additional `for` loop for scanning in the frequency domain. The second major modification is validating the presence of a fragment in line 6 in Algorithm 1. The improved model considers granularity in time and granularity in frequency. Let T_{frg} be the size of a fragment in time slots, T_{hdr} the size of a header in time slots, and F_{obw} the size of an OBW channel in frequency slots. The function `find` verifies the presence of a fragment or header in $\mathcal{M}_N$. The algorithm can determine between headers and

Algorithm 2 Proposed Doppler-compensated Greedy Headerless Decoding Heuristic.

Require: T, S, D, P and $\mathcal{M}_N$
$\mathcal{T}_C \leftarrow \{\}$
for $t \in [1;T]$ **do**
  for $s \in S$ **do**
    for $d \in \mathcal{D}$ **do**
      $found \leftarrow true$
      for $p \in [1;P]$ **do**
        if $find(\mathcal{M}_N, t, s, p, d) \neq 1$ **then**
          $found \leftarrow false$
        end if
      end for
      if $found = true$ **then**
        $\mathcal{T}_C \leftarrow \mathcal{T}_C \cup \{(s,t,P)\}$
      end if
    end for
  end for
  return $\mathcal{T}_C$
end for

Table 1
Simulation parameters.

Carrier frequency f_c	868.1 MHz
OCW actual bandwidth f^a_{ocw}	136.7 kHz
OCW RX bandwidth f^r_{ocw}	200 kHz
OBW bandwidth f_{obw}	488.28125 Hz
FHS set size S	384 sequences
Minimum payload length P_{min}	8 fragments
Maximum payload length P_{max}	31 fragments
Simulation time T	500 time slots
Fragment time t_{frg}	102.4 ms
Header time t_{hdr}	233.472 ms
Fragment size T_{frg}	6 time slots
Header size T_{hdr}	14 time slots
OBW size F_{obw}	25 frequency slots
Coding rate CR	CR1
Satellite altitude H	600 km
Maximum end-device to satellite distance D	1500 km
End-device antenna gain G_t	2.5 dBi
Gateway antenna gain G_r	22.6 dBi
End-device transmission power P_t	14 dBm
Minimum SNR	10 dB
Time slot duration t_{frg}/T_{frg}	17 ms
Frequency slot size f_{obw}/F_{obw}	20 Hz

fragments from p. Assuming the Coding Rate is known, the number of header replicas H_r is known, and then the frequency channel $s[p]$ corresponds to a header if $p \leq H_r$. Then, the function `find` function will verify if the block of size (T_{hdr}, F_{obw}) is present in $\mathcal{M}_N$ for each header and then it will verify if the block of size (T_{frg}, F_{obw}) is present in $\mathcal{M}_N$ for each fragment.

4.2.4. Payload Decoder

The Payload Decoder module is based on the traditional LR-FHSS decoder but with two different approaches. In addition to the data matrix $\mathcal{M}_N$ stored in the buffer memory, the module receives the set of transmissions with decoded headers $\mathcal{T}_S$ and an estimated set of transmissions with lost headers $\hat{\mathcal{T}}_C$. Therefore, information on the location of the payload fragments is available, and the remaining task is to retrieve the payload fragments from $\mathcal{M}_N$. The Payload Decoder can achieve this using two possible approaches.

Classic decoding. The first decoding strategy is to retrieve the payloads associated with $\mathcal{T}_S$ only. This is the same as the original LR-FHSS decoder mechanism.

Exhaustive decoding. The second decoding strategy retrieves payloads associated with $\hat{\mathcal{T}}_C$. The proposed decoder design tries to decode with both coding rates CR1 and CR2, successfully retrieving every new payload fragment until the packet is decoded.

5. Evaluation

We conducted extensive computer simulations under a series of assumptions to validate the proposed Enhanced Decoder architecture. The main objective is to quantitatively determine the advantages of implementing the Enhanced LR-FHSS receiver to improve the overall throughput in any LR-FHSS network, terrestrial or space. The results presented in this section are based on the Collision-Centric model presented in Section 3.2. The remainder of this section is organized as follows. First, the simulation environment and simulation parameters are presented. Then, the metrics used for evaluation are described. Lastly, the results are presented and analyzed based on the modules of the Enhanced LR-FHSS Receiver.

5.1. Environment

The simulation environment comprises a specific simulator adapted to space and terrestrial LR-FHSS scenarios with realistic parameters and assumptions.

Simulator. Our LR-FHSS network simulator is implemented in Python.[1] Its main objective is to study collisions based on an abstraction of the physical layer. We represent each header and fragment as a squared signal in time–frequency dimensions. This approximation originates from the constant envelope signal transmitted by an LR-FHSS end device and its ultra-narrow band communication while considering a non-selective channel for each signal.

Scenarios. The simulated LR-FHSS network comprises a single gateway receiving LR-FHSS transmissions from a population of end devices. The network module collects all frames, constructs a time–frequency matrix, accounting for Doppler effects, and delivers it to the gateway. The gateway then executes the decoding process. We consider two scenarios: space (satellite) and terrestrial. In the space scenario, the gateway is located on board the LEO satellite and the end devices are fixed on the ground, as in Fig. 1. At the moment of transmission, each end device is located under the satellite's footprint, with a maximum distance of $D = 1500$ km. The gateway is static and located on the ground in the terrestrial scenario. This represents a generic terrestrial scenario without mobility and hence no Doppler shift. We opted not to specify further details, such as urban or rural environments, because this study focuses on the core mechanisms of headerless frame recovery and not on the specific propagation conditions of various terrestrial scenarios. This approach allows us to isolate the behavior of LR-FHSS in a simplified setting, laying the groundwork for future studies that could examine more complex, location-specific conditions.

Parameters. The simulation parameters are listed in Table 1. The number of transmissions varies between 10 and 1000 during the reception window. We use the parameters described by the LoRa Regional Parameters for the European Region [10]. Each end device chooses a random number of fragments to send at a random time, both values being uniformly distributed. An LR-FHSS fragment is equivalent to T_{frg} time slots, which results in a time slot of $t_{frg}/T_{frg} \approx 17$ ms, and each LR-FHSS header is equivalent to T_{hdr} time slots. Each OBW channel is subdivided into F_{obw} frequency slots, which results in a frequency slot of $f_{obw}/F_{obw} \approx 20$ Hz. In our power-centric model, we assume that devices maintain line-of-sight communication with the satellite

[1] Our LR-FHSS network simulator available in Github: https://github.com/diegomm6/lr-fhss_seq-families.

and that the receiver on the satellite has sufficient link budget to receive transmissions under these conditions successfully. All end devices use the same coding rate CR and transmission power P_t. All transmissions start and end during the simulation time T. This ensures that all frames are complete inside the sampled matrix $\mathcal{M}_N$.

The selection of the frequency slot size reflects a trade-off between model accuracy and computational complexity. From Fig. 5, the maximum Doppler shift between fragments is approximately 25 Hz, based on a maximum Doppler Rate of 250 Hz/s. However, the Doppler shift between two consecutive fragments can be much smaller, meaning finer frequency slots would be necessary to capture the precise impact of the Doppler Rate during the transmission of an LR-FHSS packet. Although a frequency slot of 20 Hz does not fully capture the finer details of the Doppler Rate, the Doppler shift is still consistently present, and its behavior can be reliably predicted based on the satellite's altitude.

5.2. Metrics

Transmission outcome. The main metric we care to analyze is quantifying the possible LR-FHSS transmission outcomes. These are classified as follows:

- n_1: Successfully decoded header and payload.
- n_2: Successfully decoded header but collided payload.
- n_3: Collided header but retrievable payload.
- n_4: Collided header and collided payload.

For a total number of transmissions $N = n_1 + n_2 + n_3 + n_4$, the number of transmissions for each outcome is noted as n_1, n_2, n_3 and n_4, respectively. Thus, the number of transmissions whose header is successfully decoded is represented by $S = n_1 + n_2$ while the number of transmissions whose header resulted in a collision is represented by $C = n_3 + n_4$. The usual decoding process of a traditional LR-FHSS receiver allows us to decode n_1 frames among S. We aim to quantify $n_1 + n_3$, which indicates the effectively decodable frames within N.

Channel occupancy. The channel occupancy measures the average usage of a large frequency band. The channel occupancy is calculated as the average usage of each OBW over a specific time window. We focus on an extended 200 kHz OCW reception window instead of the 137 kHz OCW transmission window to account for the spread due to the Doppler shift. The channel occupancy is calculated as in Eq. (4):

$$occ(M_N) = average(bin(\mathcal{M}_N)), \tag{4}$$

where $bin(\mathcal{M}_N)$ is the binarized version of the $\mathcal{M}_N$ matrix and $average()$ calculates the mean over the whole matrix.

F1 score. The F1 score is a metric commonly used in classification tasks. It combines both precision and recall into a single value, providing a balance between these two metrics. It is calculated as the harmonic mean, with equal weight, of precision and recall as follows:

$$F_1 = \frac{2 \times precision \times recall}{precision + recall}. \tag{5}$$

The precision measures the accuracy of optimistic predictions (true positives out of all predicted positives) as given by Eq. (6). In contrast, the recall identifies all relevant instances (true positives out of all actual positives) as given by Eq. (7). The F1 score ranges from 0 to 1, where 1 indicates perfect precision and recall, and 0 indicates poor performance. Specifically, precision and recall are defined as follows:

$$precision = \frac{tp}{tp + fp}. \tag{6}$$

$$recall = \frac{tp}{tp + fn}, \tag{7}$$

where tp are the true positives, fp are the false positives and fn are the false negatives.

5.3. Results analysis

5.3.1. Transmission outcome

Fig. 7 shows the statistics of the LR-FHSS transmission outcome for each space and terrestrial scenario. A traditional LR-FHSS receiver can only decode the frames with successful header and payload receptions. This is plotted in the blue curve labeled `decoded hdr & pld (n1)`. The green curve, labeled as `decodable pld (n3)`, represents the frames whose payload could have been retrieved by the legacy LR-FHSS receiver but are dropped due to missing header parts. The yellow curve, labeled as `decoded hdr (n2)`, represents the frames whose header part was successfully decoded but the payload decoding was unsuccessful due to collisions. Lastly, the red curve, labeled as `collided hdr & pld (n4)`, are the frames whose header and payload parts are collided.

Space scenario. The proposed enhanced LR-FHSS receiver can decode both frames and thus nearly double the decoding rate depending on how saturated the channel is. Results in Fig. 7 show that the peak amount of decoded packets for the space scenario is 90 for 150 transmissions. Suppose the FHS Locator has a 100% success rate in finding all headerless packets. In that case, the decodable payloads may be added to the decoded packet, and the peak amount of the decoded packet would be 140, for a total of 200 transmissions. This represents an increase in the decoding rate of up to 50% in the space scenario.

Terrestrial scenario. On the other hand, the results for the terrestrial case in Fig. 7 show that the peak number of decoded packets is 140, for a total of 250 transmissions. If the FHS Locator has a 100% success rate, then the decodable payloads peak for a total decoded packets of 230 for 300 transmissions. This also represents a 50% increase in the terrestrial case.

Scenario comparison. It should be noted that up to 60% more frames can be decoded in the terrestrial scenario compared to the space scenario. This difference is attributed to the higher collision probability in the space scenario, where the high absolute Doppler shift increases the likelihood of frame collisions. While the variation of the frequency shift within a single LR-FHSS packet is negligible, the cumulative effect of the Doppler shift across multiple packets significantly impacts collision rates in the space scenario.

5.3.2. FHS Locator

Fig. 8 shows the results of the Locator modules implementing the Exhaustive FHS search Algorithm 2 in terms of true positives tp, false positives fp and false negatives fn. The figure presents space and terrestrial simulations. Note that the fluctuations observed in the plots are a product of the inherent randomness in the simulations, with ten iterations per data point. Despite this variability, the overall trends are consistent, providing reliable insights into performance.

Space scenario. The estimation of C is given by $\hat{C} = tp + fp$. The $\hat{C}$ estimation almost matches C up to 800 transmissions in the space use case. This is due to the low false positive and false negative rates. The explanation is that the additional frequency shift dimension makes LR-FHSS transmissions unique. Even if two transmissions choose the same sequence and transmit simultaneously, it is still improbable that they would be generated by nearby end devices, thus having a similar Doppler Shift. However, as mentioned, the higher dimensionality increases the algorithm complexity and, thus, the search time.

Terrestrial scenario. In the terrestrial case, a slight increase in the false positive rate can be noted while the false negative rate remains low. Overall, the estimation $\hat{C} = tp + fp$ always contains some false positives in the terrestrial scenario. However, the FHS Locator search algorithm for the terrestrial scenario is faster to execute due to the lower complexity. Attempting to decode false positives hinders the enhanced receiver's overall performance of the decoding process. Thus, the FHS Locator should not be applied in cases where the false positive rate is too high concerning the target C.

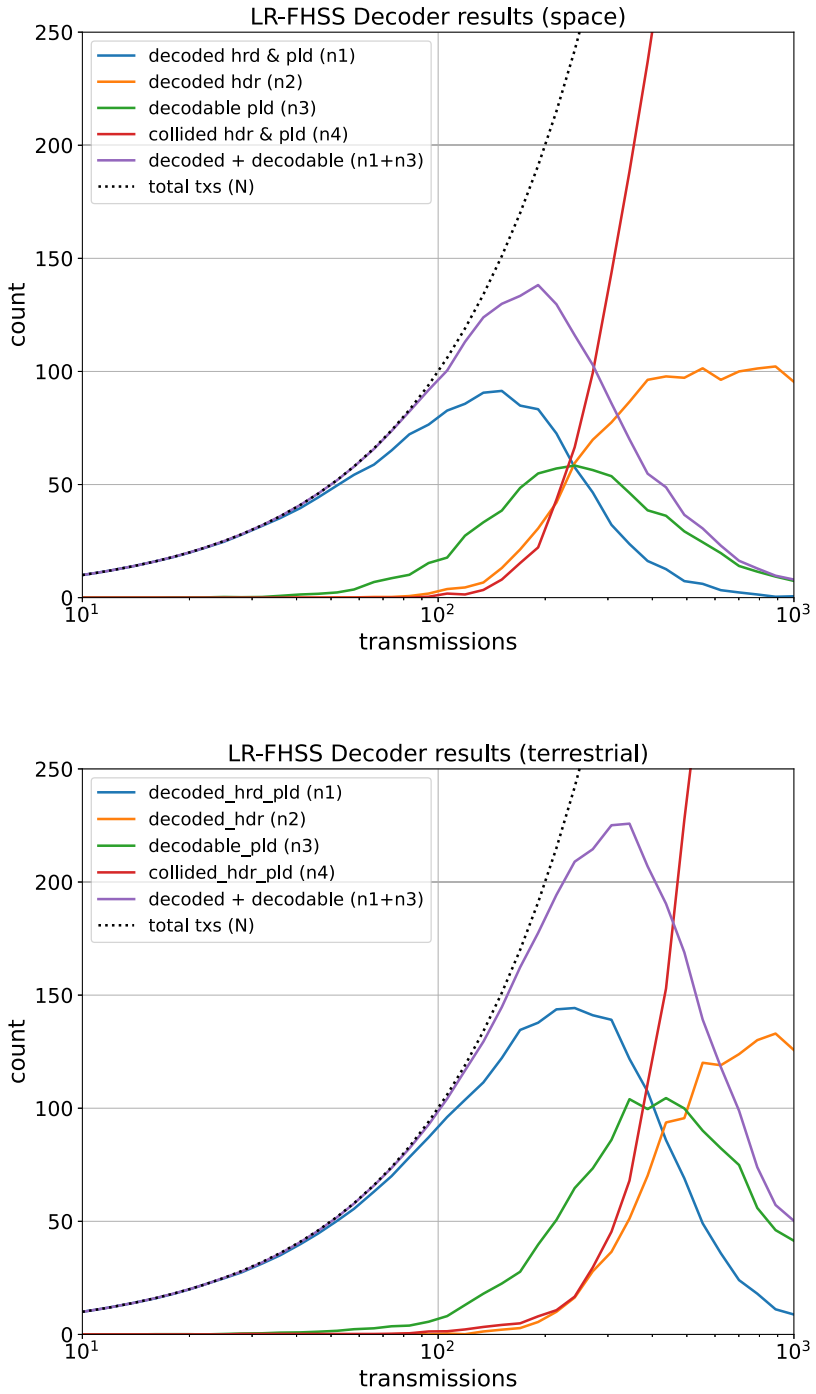

Fig. 7. LR-FHSS Decoder results for space (top) and terrestrial (bottom) scenarios. (For interpretation of the references to color in this figure legend, the reader is referred to the web version of this article.)

Scenario comparison. The results prove the proposed approach's effectiveness in finding nearly all sequences with high tp and low fn and fp rates. However, in the terrestrial case, the inability to differentiate frames using the Doppler reading causes a steep increase in false positives. This suggests that the space scenario allows our headerless decoding scheme to provide its best decoding gain. This is crucial as the space scenario poses the largest scalability challenges. We can also notice that in both scenarios, there are no collisions for small end-device populations (up to 20 end-devices). The difference matrix $\mathcal{M}_C$, computed as explained in 4.2.3, is then empty. In this case, the FHS Locator algorithm is not executed, and this module has no output data. Therefore, some blank spaces can be seen at the beginning of the plots showing results from this module.

5.3.3. F1 score

The classification performance is better appreciated with the F1 score. Fig. 9 shows the F1 score metric for the space scenario on top and the terrestrial scenario on the bottom. Note that the F1 score is introduced to evaluate the classification accuracy of our enhanced receiver's headerless decoding mechanism. It serves as a benchmark for assessing the receiver's ability to correctly identify and decode frames, laying the foundation for future comparisons with alternative headless recovery mechanisms.

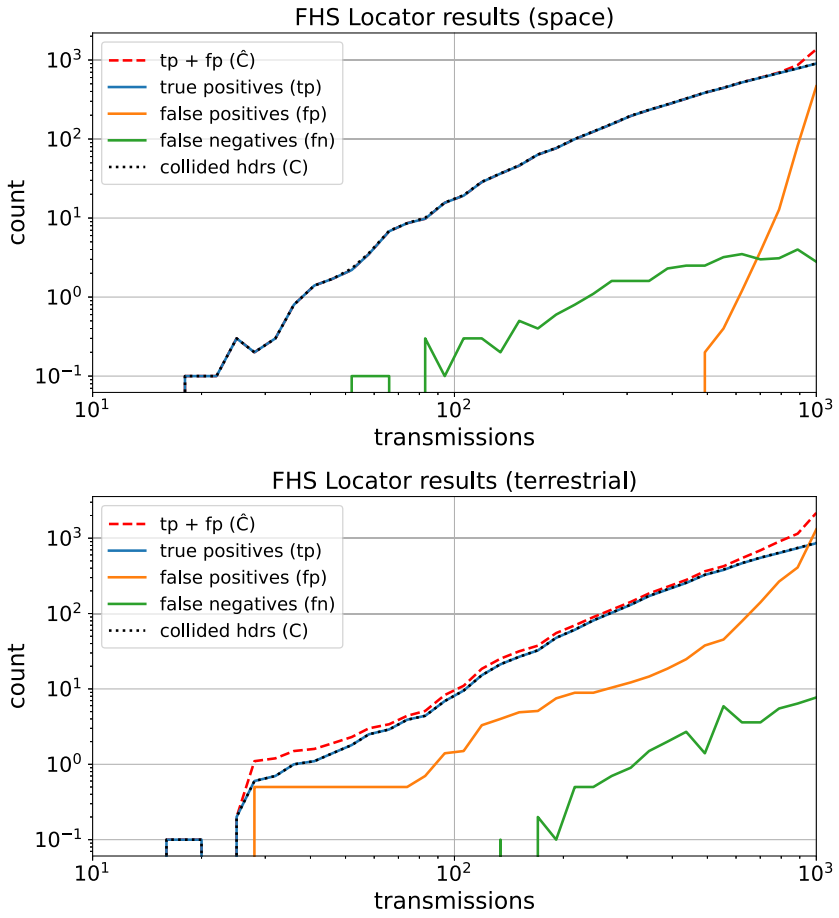

Fig. 8. FHS Locator results for space (top) and terrestrial (bottom) scenarios.

Space scenario. For the space scenario, the F1 score remains close to 1 when the number of transmissions is below 800 transmissions, indicating a near-perfect classifier, and decreases after. This is verified when comparing the F1 score curve with the false positive rate from Fig. 8 (top).

Terrestrial scenario. On the other hand, the F1 score for the terrestrial scenario is lower, a direct consequence of the lower performance of the FHS Locator module. Moreover, the F1 score decreases exponentially after 600 transmissions. This can also be verified when comparing with the false positive rate from Fig. 8 (bottom). The sudden drop of the F1 score at 30 transmissions can be explained by false positives, as seen in the false positive rate from Fig. 8 (bottom).

Scenario comparison. The comparison of both scenarios shows how the extra variable of the frequency shift helps the FHS locator rule out false positives. Hence, the FHS Locator module for the space scenario performs better.

5.3.4. Channel occupancy

We propose to evaluate the channel occupancy, as described in Section 5.2, to determine how the enhanced receiver fairs compared to the legacy receiver regarding the estimation of the number of headerless frames $\hat{C}$.

Space scenario. On the top side of Fig. 10, we show the measured channel occupancy rate compared with the retrievable payload rate $(n_1 + n_3)/N$ and the collided header estimation ratio $C/\hat{C}$. The ratio $C/\hat{C}$ is close to one until around 800 transmissions, at which point the retrievable payload rate is around 2%, and the channel occupancy is around 60%. Setting a threshold for considering the results given by the FHS Locator may also help improve the enhanced receiver's efficiency when the extra decoded payload does not justify executing the whole process. This threshold largely depends on the platform computing capabilities and the data value according to the application of the LR-FHSS network. Moreover, the receive window sampled into M_S is just a fraction of the coverage time for LEO satellite support, which can be around 10 min, depending on the elevation angle. Since the FHS locator functionality is limited to short reception windows, multiple snapshots would be retrieved over all the available OCW channels for a complete satellite pass. The small sub-estimation of C seen between 50 and 80 transmissions is explained by the false positives as seen in the false positives curve from Fig. 8 (top).

Terrestrial scenario. On the bottom of Fig. 10, it is observed how the estimation of the number of headerless packets $\hat{C}$ deviates from the target C due to the higher false positive rate. Nevertheless, the estimation remains accurate to about 80% for most end device populations before the channel becomes saturated at around 500 end devices.

Scenario comparison. The pessimistic collision model produces more collision in the terrestrial scenario. This can be noted when comparing the retrievable payload rate for both cases. The estimation $\hat{C}$ of the real amount of headerless packets is closer to its target C for the space scenario.

The results presented in this section strongly support the implementation of the proposed Enhanced LR-FHSS decoder, which would increase the frame decoding rate in any scenario, including terrestrial and space LR-FHSS networks.

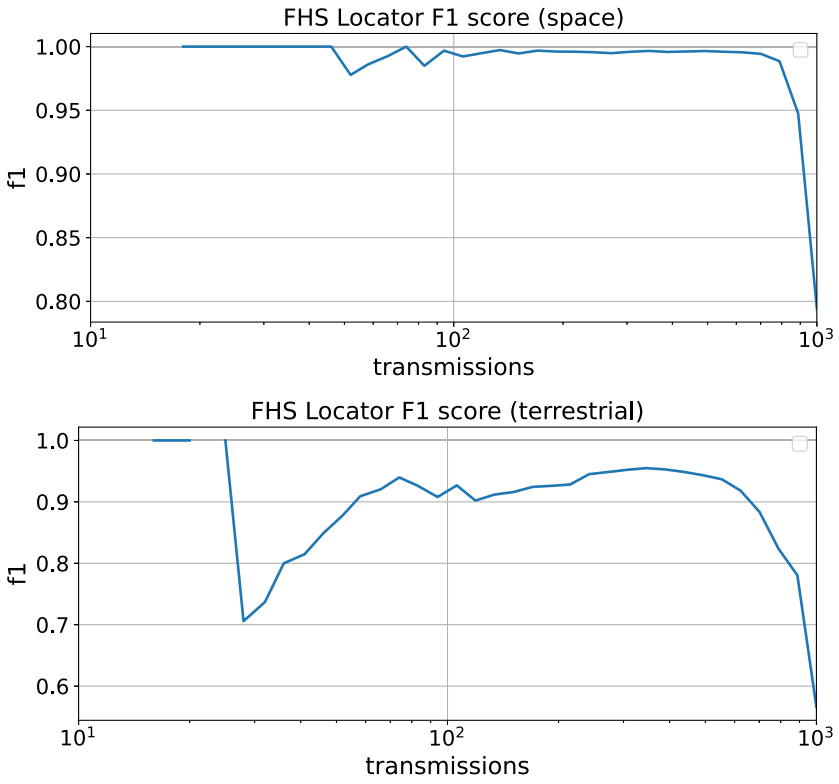

Fig. 9. FHS Locator F1 score for space (top) and terrestrial (bottom) scenarios.

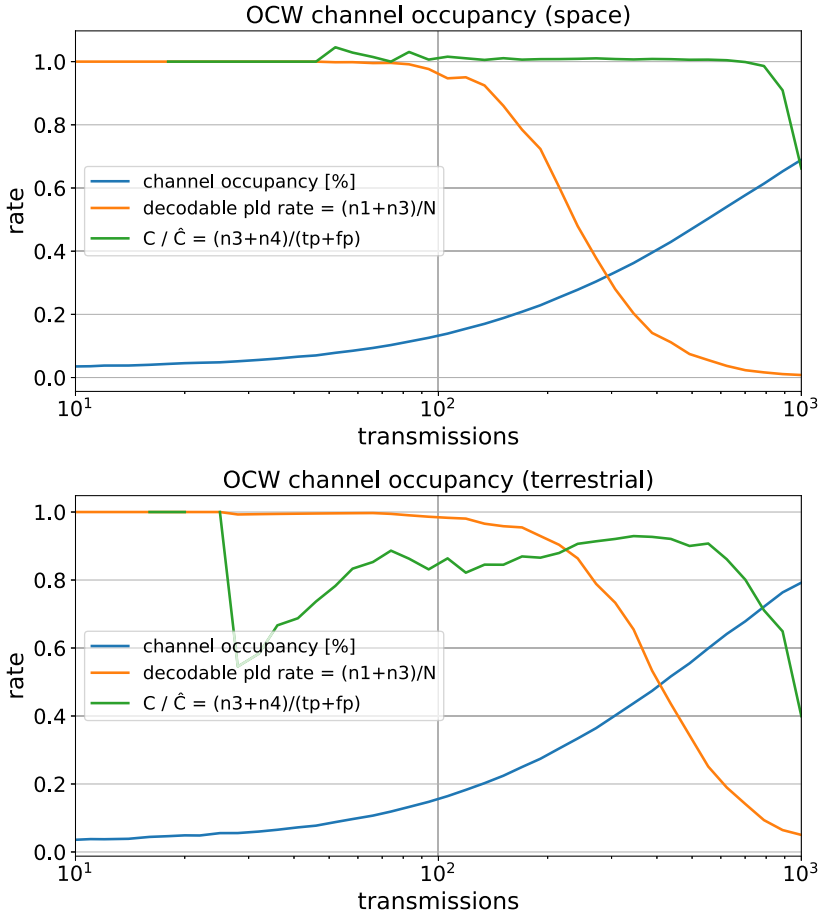

Fig. 10. Channel Occupancy for space (top) and terrestrial (bottom) scenarios.

6. Discussion

This paper presented a significant advancement in satellite IoT systems by introducing a novel Enhanced LR-FHSS Decoder architecture. Our work addresses the critical challenges of headerless frame recovery and emphasizes our solution's practical applicability in space–terrestrial integrated IoT networks. By incorporating adequate channel modeling and compensating for Doppler effects, we have substantially improved frame decoding rates, unlocking new potentials for scaling global connectivity. Communication's enhanced reliability and scalability underscore the relevance of our contributions to emerging satellite IoT systems.

Despite the notable improvements introduced by our Enhanced LR-FHSS Decoder, there are still areas that can benefit from further research and refinement. The following points outline potential directions for future work:

Physical layer modeling. We enhanced previous models by adding Doppler effects specific to LEO satellites, granularity in time and frequency, and headers in LR-FHSS frames. Although these improvements bring significant realism, refining certain assumptions could enhance accuracy. For instance, a finer model of the physical layer to simulate the capture effect in LR-FHSS packets in more detail could be beneficial. In this work, we employed a pessimistic collision approach, resulting in a lower bound of decodable packets. Nonetheless, the packets remain in the same position in the sampled M_S matrix 4.2.1, not affecting the performance of the FHS Locator module. Implementing advanced collision determination techniques, as in [29], could accurately determine how many more packets the Enhanced LR-FHSS receiver could decode.

Time modeling. Our model currently uses a fixed time window, where all frames start and end. An LR-FHSS frame may be incomplete when the spectrogram is sampled, capturing fragments whose headers are in the previous snapshot or some fragments in the following snapshot. This simplification can be easily overcome by adapting the methods discussed to operate over a sliding window technique. While this would require more buffer, it would not impact the processing time or the presented results.

FHS locator complexity. The exhaustive search algorithm's complexity is $\mathcal{O}(T \cdot S \cdot P \cdot |D|)$. For a typical satellite flyover, the coverage time can be up to 10 min, and considering multiple OCW channels, the gateway could collect hundreds of seconds worth of spectrograms. While modern nano-satellites equipped with high-performance COTS processors can handle this data, it may be impractical for resource-constrained satellite platforms based on microcontrollers. Future work could explore alternative search algorithms using advanced techniques, as in [34], to achieve faster processing times in constrained gateways.

7. Conclusions

This work introduces a novel Enhanced LR-FHSS Decoder architecture for recovering headerless frames, significantly improving the performance of space–terrestrial integrated IoT networks. Our extensive simulations demonstrate that the enhanced decoder can increase the packet delivery ratio by up to 50% in both terrestrial and satellite scenarios. This improvement is crucial for DtS-IoT networks, where high collision rates often lead to substantial data loss.

Key results and observations include:

- Doppler Effect Consideration: By incorporating Doppler compensation techniques, our enhanced decoder effectively profits from the frequency shifts inherent in LEO satellite communications to ensure a more reliable frame recovery.
- FHS Locator Accuracy: The proposed FHS Locator module accurately identifies headerless frames, maintaining a near-perfect F1 score in low to moderate transmission densities.
- Scalability: The enhanced decoder proves particularly beneficial in high-density and highly dynamic satellite IoT scenarios, where traditional LR-FHSS receivers struggle.
- Realistic Channel Modeling: By simulating realistic space-terrestrial communication environments, including variable payload sizes and partial header losses, we validated the robustness and adaptability of our enhanced decoder under practical conditions.

These advancements lay a solid foundation for the next generation of scalable and efficient space–terrestrial integrated IoT networks based in LR-FHSS, promising substantial improvements in communication reliability and network performance.

Further research will explore advanced collision determination techniques and adaptive decoding strategies to maximize the potential of LR-FHSS networks. Additionally, we plan to investigate collaborative headerless decoding among multiple receiving gateways, each perceiving a different Doppler profile. As a next step, we aim to explore the possibility of conducting experiments with LR-FHSS frames, either from ground-based testbeds or from real satellites, as opportunities arise, to further validate the Enhanced LR-FHSS Receiver with real-world data, though access to such resources remains a significant challenge.

CRediT authorship contribution statement

Diego Maldonado: Writing – review & editing, Writing – original draft, Software, Resources, Methodology, Investigation, Conceptualization. **Leonardo S. Cardoso:** Writing – original draft, Methodology, Investigation, Conceptualization. **Juan A. Fraire:** Writing – review & editing, Writing – original draft, Validation, Supervision, Conceptualization. **Alexandre Guitton:** Writing – original draft, Investigation, Formal analysis, Conceptualization. **Oana Iova:** Resources, Project administration, Methodology, Investigation. **Megumi Kaneko:** Methodology, Investigation, Conceptualization. **Hervé Rivano:** Investigation, Funding acquisition, Conceptualization.

Declaration of competing interest

The authors declare that they have no known competing financial interests or personal relationships that could have appeared to influence the work reported in this paper.

Acknowledgments

This research has received support from the European Union's Horizon 2020 R&D program under the Marie Skłodowska-Curie grant agreement No 101008233 (MISSION project), the French National Research Agency (ANR) under the projects ANR-22-CE25-0014-01 and ANR-21-CE25-0002-01, the Grant-in-Aid for Scientific Research (Kakenhi 22KK0156) from the Ministry of Education, Science, Sports, and Culture of Japan, and by the JST ASPIRE Grant Number JPMJAP2325 in Japan.

Data availability

No data was used for the research described in the article.

References

[1] J.A. Fraire, S. Céspedes, N. Accettura, Direct-to-satellite IoT-a survey of the state of the art and future research perspectives: Backhauling the IoT through LEO satellites, in: ADHOC-now 2019, Proceedings 18, Springer, 2019, pp. 241–258.
[2] J.A. Fraire, S. Henn, F. Dovis, R. Garello, G. Taricco, Sparse satellite constellation design for lora-based direct-to-satellite internet of things, in: GLOBECOM 2020-2020 IEEE Global Communications Conference, IEEE, 2020, pp. 1–6.
[3] J. Zhang, Y. Cai, C. Xue, Z. Xue, H. Cai, LEO mega constellations: review of development, impact, surveillance, and governance, Space: Sci. Technol. (2022).
[4] F. Gu, J. Niu, L. Jiang, X. Liu, M. Atiquzzaman, Survey of the low Power Wide Area network technologies, J. Netw. Comput. Appl. 149 (2020) 102459.

[5] J.A. Fraire, O. Iova, F. Valois, Space-terrestrial integrated internet of things: Challenges and opportunities, IEEE Comms. Mag. (2022).
[6] C. Vincent, B.J. Mcconnell, V. Ridoux, M.A. Fedak, Assessment of argos location accuracy from satellite tags deployed on captive gray seals, Mar. Mam. Sci. 18 (1) (2002) 156–166.
[7] R. Patmasari, I. Wijayanto, R. Deanto, Y. Gautama, H. Vidyaningtyas, Design and realization of automatic packet reporting system (APRS) for sending telemetry data in nano satellite communication system, J. Meas. Electron. Commun. Syst. 4 (1) (2018) 1–7.
[8] J. Carson-Jackson, Satellite AIS – developing technology or existing capability? J. Navig. 65 (2) (2012) 303–321.
[9] K. Werner, J. Bredemeyer, T. Delovski, ADS-b over satellite: Global air traffic surveillance from space, in: 2014 Tyrrhenian International Workshop on Digital Communications-Enhanced Surveillance of Aircraft and Vehicles (TIWDC/ESAV), IEEE, 2014, pp. 47–52.
[10] Semtech, Application note: LR-FHSS system performance, 2022, pp. 1–28, Available at https://www.mouser.com/pdfDocs/AN1200-64_LR-FHSS_system_performance_V1_2.pdf. (17 April 2023).
[11] G. Boquet, P. Tuset-Peiró, F. Adelantado, T. Watteyne, X. Vilajosana, LR-FHSS: Overview and performance analysis, IEEE Commun. Mag. 59 (3) (2021) 30–36.
[12] M.A. Ullah, K. Mikhaylov, H. Alves, Analysis and simulation of lorawan LR-FHSS for direct-to-satellite scenario, IEEE Wirel. Commun. Lett. 11 (3) (2022) 548–552.
[13] A. Maleki, H.H. Nguyen, E. Bedeer, R. Barton, Outage probability analysis of LR-FHSS and D2D-aided LR-FHSS protocols in shadowed-rice fading direct-to-satellite IoT networks, IEEE Internet Things J. 11 (6) (2024) 11101–11116.
[14] J.A. Fraire, A. Guitton, O. Iova, Recovering headerless frames in LR-FHSS, in: Proceedings of the 2023 International Conference on Embedded Wireless Systems and Networks, EWSN '23, Association for Computing Machinery, New York, NY, USA, 2023, pp. 170–180.
[15] M. Capuzzo, C. Delgado, A.K. Sultania, J. Famaey, A. Zanella, Enabling green IoT: Energy-aware communication protocols for battery-less LoRaWAN devices, in: Proceedings of the 24th International ACM Conference on Modeling, Analysis and Simulation of Wireless and Mobile Systems, 2021, pp. 95–98.
[16] M.A. Ullah, K. Mikhaylov, H. Alves, Analysis and simulation of lorawan LR-FHSS for direct-to-satellite scenario, IEEE Wirel. Commun. Lett. 11 (3) (2021) 548–552.
[17] A. Maleki, H.H. Nguyen, R. Barton, Outage probability analysis of LR-FHSS in satellite IoT networks, IEEE Commun. Lett. 27 (3) (2022) 946–950.
[18] R. Sanchez-Vital, L. Casals, B. Heer-Salva, R. Vidal, C. Gomez, E. Garcia-Villegas, Energy performance of LR-FHSS: analysis and evaluation, 2024, arXiv preprint arXiv:2408.04908.
[19] S. Jung, S. Jeong, J. Kang, G. Im, S. Lee, M.-K. Oh, J.G. Ryu, J. Kang, LR-FHSS transceiver for direct-to-satellite IoT communications: Design, implementation, and verification, 2024, arXiv preprint arXiv:2403.14154.
[20] J.M. de Souza Sant'Ana, A. Hoeller, H. Alves, R.D. Souza, LR-FHSS-sim: A discrete-event simulator for LR-FHSS networks, in: 2024 Joint European Conference on Networks and Communications & 6G Summit (EuCNC/6G Summit), IEEE, 2024, pp. 700–705.
[21] D.N. Knop, J.L. Rebelatto, R.D. Souza, LR-FHSS with network-coded header replication, IEEE Trans. Veh. Technol. (2024).
[22] J.M. de Souza Sant'Ana, O. da Silva Neto, A. Hoeller, J.L. Rebelatto, R.D. Souza, H. Alves, Asynchronous contention resolution-aided ALOHA in LR-FHSS networks, IEEE Internet Things J. (2024).
[23] M.A. Ullah, K. Mikhaylov, H. Alves, Experiment-based models for air time and current consumption of lorawan LR-FHSS, 2024, arXiv preprint arXiv:2408.09954.
[24] D. Maldonado, M. Kaneko, J.A. Fraire, A. Guitton, O. Iova, H. Rivano, Enhancing LR-FHSS scalability through advanced sequence design and demodulator allocation, 2024, arXiv preprint arXiv:5709290.5709290. [Online]. Available: URL https://arxiv.org/submit/5709290.
[25] F. Zhang, F. Yu, X. Zheng, L. Liu, H. Ma, DFH: Improving the reliability of LR-FHSS via dynamic frequency hopping, in: 2023 IEEE 31st International Conference on Network Protocols, ICNP, 2023, pp. 1–12.
[26] D. Wang, A. Elzanaty, M.-S. Alouini, Coded frequency hopping for direct-to-satellite IoT systems: Design and analysis, IEEE Internet Things J. (2024) 1–1.
[27] D.N. Knop, J.L. Rebelatto, R.D. Souza, LR-FHSS with network-coded header replication, IEEE Trans. Veh. Technol. 73 (6) (2024) 9066–9070.
[28] S. Jung, S. Jeong, J. Kang, J.G. Ryu, J. Kang, Transceiver design and performance analysis for LR-FHSS-based direct-to-satellite IoT, IEEE Commun. Lett. 27 (12) (2023) 3310–3314.
[29] M.A.B. Temim, G. Ferré, O. Seller, An LR-FHSS receiver for a massive IoT connectivity, in: 2023 IEEE 34th Annual International Symposium on Personal, Indoor and Mobile Radio Communications, PIMRC, IEEE, 2023, pp. 1–6.
[30] SEMTECH, AN1200.22 LoRa™ modulation basics, 2023, Available at https://semtech.my.salesforce.com/sfc/p/#E0000000JelG/a/2R0000001OJk/yDEcfAkD9qEz6oG3PJryoHKas3UMsMDa3TFqz1UQOkM. (17 April 2023).
[31] M.A. Ullah, G. Pasolini, K. Mikhaylov, H. Alves, Understanding the limits of LoRa direct-to-satellite: The Doppler perspectives, IEEE Open J. Commun. Soc. (2023).
[32] LoRaAlliance, RP002-1.0.3 LoRaWAN® regional40 parameters, 2023, Available at https://hz137b.p3cdn1.secureserver.net/wp-content/uploads/2021/05/RP002-1.0.3-FINAL-1.pdf?time=1681357388. (17 April 2023).
[33] I. Ali, N. Al-Dhahir, J.E. Hershey, Doppler characterization for LEO satellites, IEEE Trans. Commun. 46 (3) (1998) 309–313.
[34] G. Li, W. Wang, G. Ding, Q. Wu, Z. Liu, Frequency-hopping frequency reconnaissance and prediction for non-cooperative communication network, China Commun. 18 (12) (2021) 51–64.

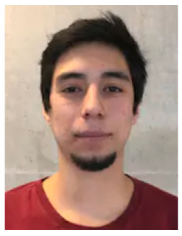

Diego Maldonado has been a PhD Student at INSA Lyon (France) and INRIA (France) since 2023. He received his M.Sc. from the University Paris-Scaly in 2021 and his M.Sc. in Computer Science from the University of Chile in 2022. His research is in the Internet of Things, Direct to Satellite IoT, with a focus on LoRa-based DtS IoT networks.

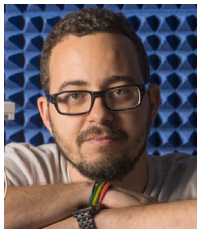

Leonardo S. Cardoso is an associate professor at INSA Lyon. He received his M.Sc. degree from the Universidade Federal do Ceará, Brazil, 2006 and his Ph.D. in 2011 at Supélec, France, on Dynamic Spectrum Access. He is the lead researcher responsible for France's CorteXlab wireless experimental testbed. His research interests include deep learning for wireless communications, signal processing, and interference management.

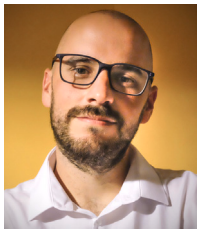

Juan A. Fraire is a researcher at INRIA (France) and a guest professor at CONICET-UNC (Argentina) and Saarland University (Germany). Core topics of his interest are near-Earth and deep-space networking and informatics, adding up to more than 100 published papers in international journals and leading conferences. Juan is the co-founder and chair of the space–terrestrial Internetworking Workshop (STINT) and participates in diverse joint projects with space agencies (e.g., NASA, ESA, CONAE) and companies in the space sector (e.g., D3TN, Skyloom).

Alexandre Guitton has been a professor at Clermont Auvergne INP, Université Clermont Auvergne, France, since 2018. Previously, he was an associate professor (from 2014–2018) and assistant professor (from 2007–2014) at the same university. He obtained his PhD from Université de Rennes I (France) in 2005 and his MSc from Université de Rennes I (France) in 2003. His research focuses on low-power wide area networks, especially LoRa / LoRaWAN protocols. Notably, he is working on decoding collided LoRa frames and optimizing demodulator allocation in LoRaWAN gateways.

Oana Iova is associate professor at INSA Lyon, France since 2017. She received her Ph.D. in computer science from University of Strasbourg, France in 2014 and her M.Sc. from École Normale Supérieure de Lyon, France in 2011. Her research is in performance evaluation, routing and MAC protocols for wireless networks, with a focus on low-power long-range technologies for the Internet of Things.

Megumi Kaneko (S'06, M'08, SM'17) received her Diplôme d'Ingénieur from Télécom SudParis (French Grande Ecole), France, in 2004, jointly with a MSc. degree from Aalborg University, Denmark, where she received her Ph.D. degree in 2007. In May 2017, she obtained her HDR degree (French Doctoral Habilitation for Directing Research, at Professor position) from Paris-Saclay University, France. She was a JSPS post-doctoral fellow at Kyoto University from April 2008 to August 2010. From September 2010 to March 2016, she was an Assistant Professor in the Department of Systems Science, Graduate School of Informatics, Kyoto University.

From April 2016 to March 2024, she was an Associate Professor at the National Institute of Informatics (NII) and the Graduate University for Advanced Studies (Sokendai), Tokyo, Japan, where she is now a full Professor since April 2024. Her research interests include wireless communications, PHY/MAC design and optimization, energy efficiency, and IoT massive connectivity for Beyond 5G. She is an IEEE Transactions on Wireless Communications, IEEE Communications Letters, and IEEE Wireless Communications Letters Editor. Since September 2020, she has been a member of the Advisory Board for Promoting Science and Technology Diplomacy at Japan's Ministry of Foreign Affairs. She received the 2009 Ericsson Young Scientist Award, the IEEE Globecom 2009 Best Paper Award, the 2011 Funai Young Researcher's Award, the WPMC 2011 Best Paper Award, the 2012 Telecom System Technology Award, the 2016 Inamori Foundation Research Grant, the 2019 Young Scientist Prize from the Minister of Education, Culture, Sports, Science and Technology of Japan, the 2020 IEEE Communications Letters Exemplary Editor Award and the 2021 KDDI Foundation Contributions Award. She is a Senior Member of IEEE

Hervé Rivano is a Full Professor at INSA Lyon and the head of the Inria/INSA Lyon common team Agora of the CITI lab, which focuses on wireless networks in Smart Cities. He obtained his Ph.D. in November 2003 from the University of Nice-Sophia Antipolis and graduated from the Ecole Normale Supérieure de Lyon. His research interests include combinatorial optimization applied to network design and provisioning. He focuses on capacity/energy tradeoffs for urban cellular and mesh network design and low-cost and dense wireless sensor networks for environmental sensing.